

A complex storm system in Saturn's north polar atmosphere in 2018

A. Sánchez-Lavega^{1*}, E. García-Melendo², J. Legarreta³, R. Hueso¹, T. del Río-Gaztelurrutia¹, J. F. Sanz-Requena⁴⁻⁵, S. Pérez-Hoyos¹, A. A. Simon⁶, M. H. Wong⁷, M. Soria⁸, J. M. Gómez-Forrellad⁹, T. Barry¹⁰, M. Delcroix¹¹, K. M. Sayanagi¹², J. J. Blalock¹², J. L. Gunnarson¹², U. Dyudina¹³, S. Ewald¹³

1. Departamento Física Aplicada I, Escuela de Ingeniería de Bilbao, Universidad del País Vasco UPV/EHU, 48013 Bilbao, Spain (agustin.sanchez@ehu.eus)
2. Serra Hünter Fellow, Escola Superior d'Enginyeries Industrial, Aeroespacial i Audiovisual, UPC, Terrasa, Spain
3. Departamento de Ingeniería de Sistemas y Automática, Escuela de Ingeniería de Bilbao, Universidad del País Vasco UPV/EHU, 48013 Bilbao, Spain
4. Departamento de Ciencias Experimentales. Universidad Europea Miguel de Cervantes, Valladolid, Spain
5. Departamento de Física Teórica, Atómica y Óptica; Facultad de Ciencias, Universidad de Valladolid, Valladolid, Spain
6. NASA Goddard Space Flight Center, Greenbelt, MD, USA
7. University of California Berkeley, Berkeley, CA, USA,
8. Escola Superior d'Enginyeries Industrial, Aeroespacial i Audiovisual, UPC, Terrasa, Spain,
9. Fundació Observatory Esteve Duran, Barcelona, Spain
10. Broken Hill Observatory, 406 Bromide St Broken Hill NSW, Australia
11. Société Astronomique de France, Paris, France.
12. Hampton University, VA, USA
13. California Institute of Technology, Pasadena, CA, USA

*email: agustin.sanchez@ehu.eus

Saturn's convective storms usually fall in two categories. One consists of mid-sized storms ~ 2,000 km wide, appearing as irregular bright cloud systems that evolve rapidly, on scales of a few days. The other includes the exceptional Great White Spots (GWS), planetary-scale giant storms that disturb a full latitude band, and which have been observed only seven times. Here we report a new intermediate type, observed in 2018 in the North Polar Region. Four large storms (the first one lasting longer than 200 days) formed sequentially in close latitudes, experiencing mutual encounters, and leading to zonal disturbances affecting a full latitude band ~ 8,000 km wide, during at least 8 months. Dynamical simulations indicate that each storm required energies ~ 100 times smaller than those necessary for a GWS. This event occurred at about the same latitude and season as the GWS in 1960, in close correspondence with the cycle of approximately 60 years hypothesized for equatorial GWSs.

49 Saturn's convective storms of both mid and planetary scale have been imaged at optical
 50 and near infrared wavelengths from the Voyager 1 and Voyager 2 spacecrafts [1-5], the
 51 Hubble Space Telescope (HST) [6-9], ground-based telescopes, and Cassini spacecraft
 52 [10-12]. Cassini also detected radio emissions and bright flashes associated with lightning
 53 in the storms [13-16]. These storms result from moist convection in the upper cloud layers
 54 [17-18] and play a significant role in Saturn's atmospheric dynamics [11-12, 19-20].

55

56 Saturn was observed from Earth during its entire 2018 apparition. Our study concentrates
 57 in the period from March 29 (date of discovery of the first storm) to November 21. In this
 58 period, unusual bright spots emerged between latitudes 67°N and 74°N , on the north side
 59 of a double-peaked eastward jet [5, 21], reaching Saturn's hexagon border. This report is
 60 primarily based on the analysis of > 500 telescopic images obtained in the visual range,
 61 provided by a network of 81 observers contributing to the open repositories PVOL [22]
 62 and ALPO-Japan (Supplementary Table 1). Additional images in the visual and near
 63 infrared spectral ranges were obtained during three observing runs (May, June and
 64 September 2018) with the 2.2 m telescope at Calar Alto Observatory using the camera
 65 PlanetCam [23]. We have also used images obtained on June 6-7, 2018 with the Wide
 66 Field Planetary Camera (WFPC) of the Hubble Space Telescope (HST), pertaining to the
 67 OPAL program [24]. Finally, images captured between December 2016 and September
 68 2017 by the Imaging Science Subsystem (ISS) camera onboard NASA's Cassini
 69 spacecraft were used to identify a precursor of the first storm as described below. Details
 70 on the observations and image analysis are given in Methods and Supplementary
 71 Material.

72

73 **Evolution of convective storms**

74

75 The first storm WS1 ("White Spot 1") was imaged on March 29 (day $t=0\text{d}$) as a bright
 76 spot of dimensions 10° east - west and 4° north - south ($\sim 4,000$ km), at latitude 67.4°N
 77 within a region of cyclonic vorticity (Figs. 1-2, Supplementary Fig. 1). Latitudes are
 78 planetographic (φ) throughout unless otherwise noted. By 1 April ($t=3\text{d}$) the clouds had
 79 expanded westward and eastward at the north and south edges respectively, in agreement
 80 with the direction of the meridional shear of the zonal winds at this latitude [5, 21]. WS1
 81 remained a compact spot; to the east and west of WS1, other spots of smaller size and
 82 brightness formed. On May 25 ($t=56\text{d}$) a second bright spot (WS2) was observed, 30°
 83 to the west and 0.7° north of WS1. Higher resolution HST images from June 6 show that
 84 both WS1 and WS2 consist of 3-4 smaller spots from which zonally elongated filaments
 85 extend, oriented according to the meridional wind shear (Fig. 1 map, Supplementary Fig.
 86 1). By June 17-18 ($t=81\text{d}$), WS2 developed a tail, grew in longitude, and a third distinct
 87 bright spot (WS3) formed at WS2's northwest, separated by 20° in longitude and at 72°N
 88 in latitude (Fig. 1c-e). A fourth short-lived spot (WS4) formed on August 13 ($t=137\text{d}$) at
 89 latitude 74.3°N , 0.7° south of the hexagon border (Fig. 1j). We tracked WS1 and WS2
 90 until late October 2018, when the spots ceased to be detected, resulting in a lifetime of \sim
 91 214 and ~ 157 days respectively. We also measured the System III longitude drift rate of
 92 the storms and other features (ω , $^{\circ}/\text{day}$), their zonal velocities (u , ms^{-1}), and their mean
 93 latitude (φ) over their lifetime (Figure 2, Table 1, Supplementary Figures 2-3). We find
 94 that the velocities of WS2, WS3 and WS4 are very close (by 5ms^{-1}) to the zonal wind
 95 speed at their respective latitudes [5, 21]. WS1 moved about 35ms^{-1} slower than the wind
 96 profile [21]. Part of this difference could be due to the $\pm 0.7^{\circ}$ uncertainty in the latitude
 97 measurements of the storm (Supplementary Figure 3). However, we found that a cyclone
 98 that was visible north of a coupled three vortex system in 2015 HST images [25], and can

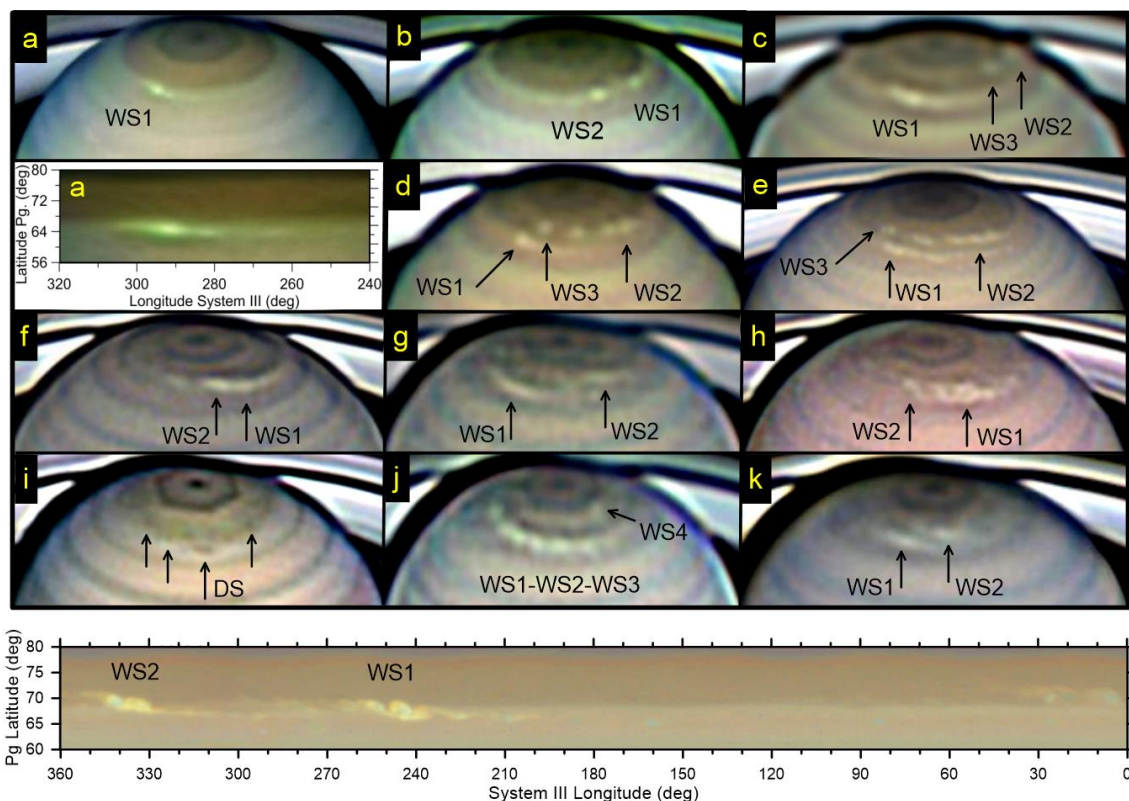
99 be traced in Cassini ISS images at least since 2013, exhibited a good match to WS1 in
 100 latitude, longitude, and drift rate during the period 2016-2017 (Figure 3). This indicates
 101 that the outbreak WS1 most probably began in that cyclone, similar to the genesis of large
 102 convective storms within cyclones observed on Jupiter [26]. Since the cyclone was
 103 located $+0.5^\circ$ to the north of WS1 mean latitude, but moved with the same velocity (Fig.
 104 3, Table 1), the cyclone moved 15 ms^{-1} slower than the zonal winds [21, and this is
 105 probably also the case for WS1 once the latitude uncertainty is taken into account.

106

107 The separation in latitude between the storms resulted in zonal velocities ranging from
 108 $+60 \text{ ms}^{-1}$ at 67°N to -5 ms^{-1} at 74°N (Figure 2, Table 1). Since the storms were close in
 109 latitude, there were mutual encounters when a faster WS1 overtook WS2 and when WS1
 110 overtook WS3 (Figure 2). The interaction between the storms during their close passages
 111 generated chains of bright spots along a longitude sector $\sim 100^\circ$ in extent ($\sim 45,000 \text{ km}$)
 112 at latitudes $+67^\circ$ and $+71^\circ$ (Fig. 1d-h, Supplementary Figure 1). Typically these chains
 113 consisted of about 7-10 spots with a mean separation of $7,500 \pm 900 \text{ km}$, suggesting that
 114 a wave disturbance was triggered during the encounters (Fig. 1j). At other longitudes
 115 where no bright spot chain formed, there appeared dark spots (such as DS in Fig. 1i) and
 116 other less contrasted spots (indicated by arrows in Fig. 1i), and by July (t $\sim 120 \text{ d}$) all
 117 longitudes in the cyclonic side of the jet, within a band from latitudes $\sim +66^\circ$ to $+73^\circ$,
 118 were disturbed (Fig. 1j).

119

120



121

122

123

124

125

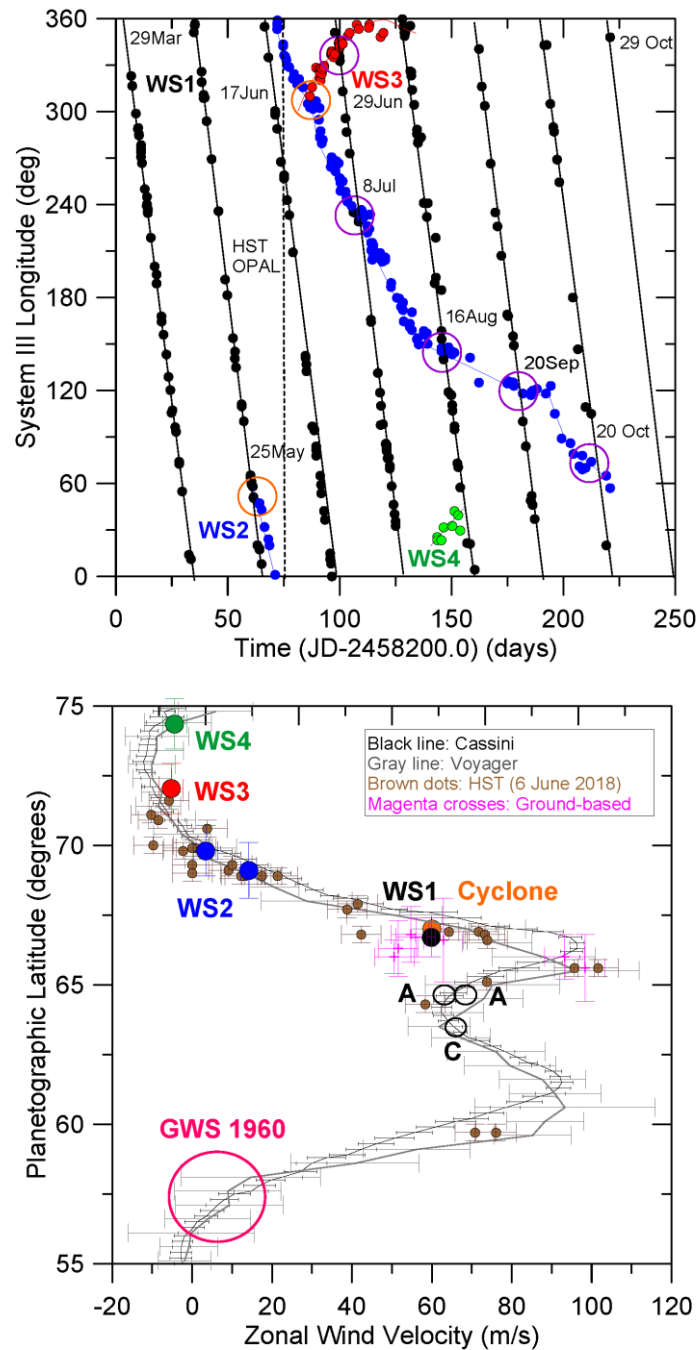
126

127

Figure 1. The 2018 complex north polar storm system and disturbances. Saturn is shown in a series of ground-based images during the 2018 apparition. Each image is cropped such that the bottom edge falls on 47°N latitude at central meridian. (a) April 1 (D. Peach) and cylindrical map projection of this image; (b) May 26 (A. Casely); (c) June 23 (T. Barry); (d) June 28 (D. Peach); (e) June 30 (D.P. Milika & P. Nicholas); (f) July

128 11 (B. Macdonald); (g) August 8 (T. Barry); (h) August 16 (F. Silva-Correa); (i) August
 129 18 (D. Peach); (j) August 19 (T. Barry); (k) September 16 (B. Macdonald). Bottom: HST
 130 cylindrical map on June 6. Identification of features follows the nomenclature given in
 131 the text. See also Supplementary Figure 1.

132



133

134

135 **Figure 2. Storm motions from March 29 to October 29, 2018.** (a) Black (storm WS1),
 136 blue (storm WS2), red (storm WS3) and green (storm WS4) show the motions of the four

137 *long-lived storms in System III longitude. Orange circles mark the date and position of*
 138 *the outbreak of WS2 and WS3. Violet circle marks the date of the close encounters*
 139 *between storms: WS1-WS3 (~29 June, $t \sim 93d$), WS1-WS2 (~8 July, $t \sim 100d$), WS1-WS2*
 140 *(~16 Aug, $t \sim 140d$), WS1-WS2 (~20 September, $t \sim 174d$), WS1-WS2 (~20 October, $t \sim$*
 141 *211d). The vertical dashed line indicates the HST observation date. (b) Zonal velocity of*
 142 *the main storms (WS1- WS4) and other features (small brown dots and magenta crosses)*
 143 *pertaining to the disturbance in the averaged wind profile [5, 21]. The orange dot*
 144 *corresponds to the cyclone where WS1 erupted. The long-lived Anticyclone-Cyclone-*
 145 *Anticyclone (ACA) triple vortex is also indicated [25]. See also Supplementary Figures*
 146 *2-3. The location of the GWS 1960 is indicated by a large pink circle [6, 12]. The upper*
 147 *graph has no error bars visible in longitude axis since they are smaller than the dot*
 148 *representing each measurement. The lower graph shows error bars in the wind profile*
 149 *from [5, 21]. The error bars in the individual velocity points from measurements of*
 150 *ground-based and HST images are calculated as follows: in velocity, using the linear fits*
 151 *to the longitude drift rates of the features, and in latitude, from the error in the planet*
 152 *limb navigation and feature pointing. The features latitude error for HST images is $\pm 0.3^\circ$*
 153 *and in ground-based images ranges from $\pm 0.7^\circ$ to $\pm 1.5^\circ$ (standard deviation from the*
 154 *mean value).*

155

156

Table 1: Main polar storms motions

Storm	Onset (2018)	Latitude φ ($^\circ$)	Drift ω ($^\circ/\text{day}$)	Zonal Velocity u (ms^{-1})	Tracking time (days)
WS1	25 Mar	$66.7^\circ \pm 0.7^\circ \text{N}$	-11.5	$+59.8 \pm 1.5$	214
WS2	25 May	$69.1^\circ \pm 1^\circ \text{N}$	-3	$+14.2 \pm 2$	157
WS2 *	25 May	$69.8^\circ \pm 0.9^\circ \text{N}$	-0.75	$+3.4 \pm 2$	157
WS3	17 Jun	$72.04^\circ \pm 0.9^\circ$	+1.3	-5.2 ± 2	33
WS4	13 Aug	$74.3^\circ \pm 0.9^\circ \text{N}$	+1.2	-4.4 ± 2	10

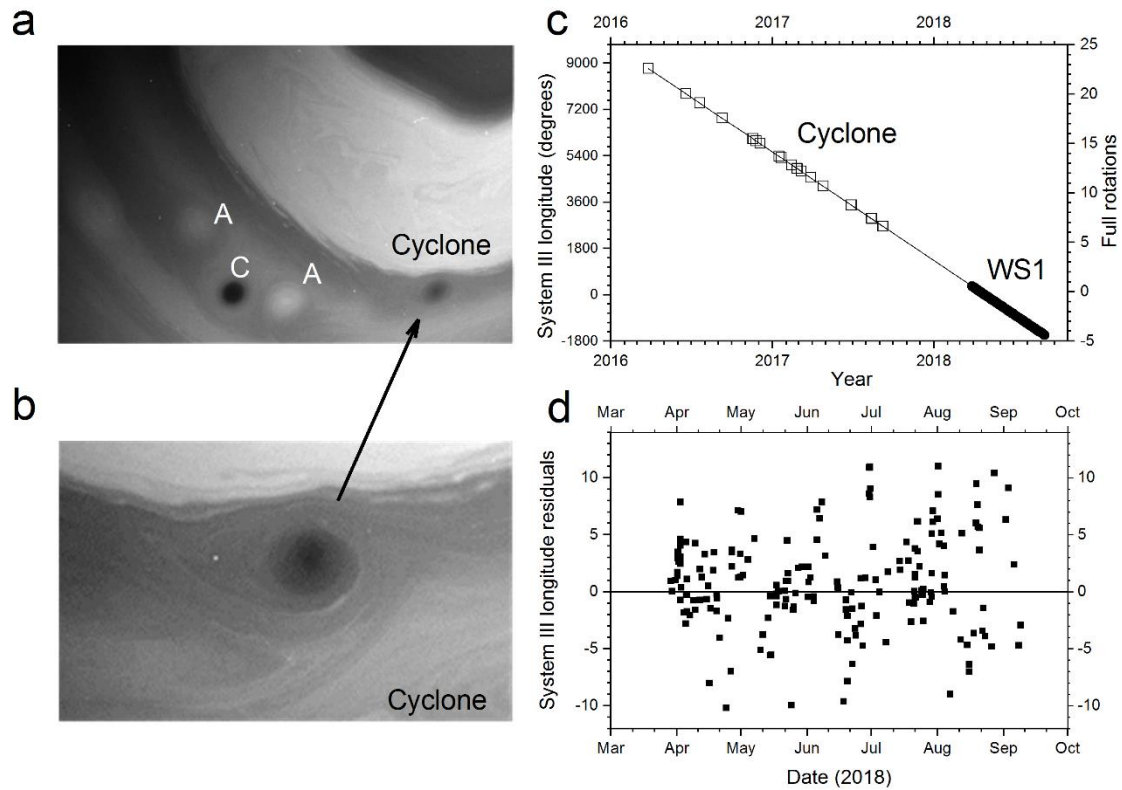
157

158

159

160

*WS2 changed in latitude (see Fig. 2 and Supplementary Fig. 2)



161
162

163 **Figure 3. Convective onset in a compact cyclone.** (a) Cassini ISS image showing the
164 ACA (Anticyclone-Cyclone-Anticyclone) system [25] and the Cyclone where WS1
165 erupted. Image obtained on March 7, 2017, using the 889 nm methane band filter (MT3)
166 [10] (Cassini image number W1867560436_1.IMG). (b) Detail showing the Cyclone.
167 Image obtained on February 13, 2007, using the same filter (Cassini image number
168 W1865704116_1.IMG) (c) Longitude drift of the Cyclone (squares) and WS1 (dark spots)
169 and linear fit to the data. A total of 39 images of the cyclone were used spanning the
170 period from March 25, 2016 to September 08, 2017. (d) Residuals in System III longitude
171 between the extended linear fit of the Cyclone drift and the measured longitude of the
172 storm WS1. No error bars in longitude axis are shown in c since they are similar to the
173 size of the dot representing each measurement.

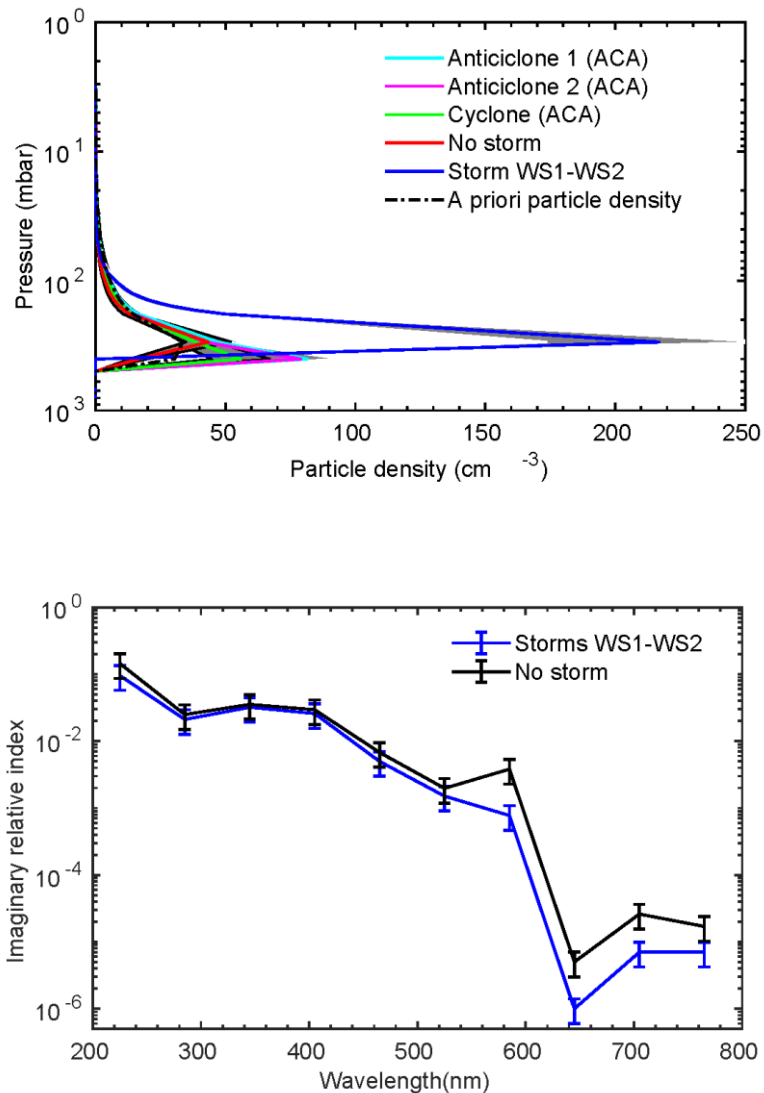
174

175 Vertical structure of storm clouds

176

177 HST images obtained at different wavelengths (Supplementary Figure 4) were calibrated
178 in absolute reflectivity (I/F , intensity/solar flux, as it is conventional in planetary
179 atmospheres) [27] and we retrieved center to limb dependence of I/F at each available
180 wavelength both for the storms and adjacent undisturbed areas. We used the NEMESIS
181 radiative transfer code [28] to model the upper cloud structure and hazes [29] (Methods
182 and Supplementary Figure 5). The wavelength range covered by HST images allows
183 sounding the tropospheric haze and the top level of the upper ammonia cloud [30-31].
184 When comparing the storm cloud structure to the surrounding clouds, the model fit to the
185 observations is improved if the storm clouds are denser and slightly higher. The storm
186 model requires an increase in the optical depth of the tropospheric cloud from ~ 10 to 32
187 (i. e. an increase in the particle density from ~ 50 to 215 cm^{-3}) together with an increase
188 in the top altitude of the hazes from ~ 600 to 200 mbar (Figure 4, Supplementary Tables
189 2-3). Height of the storm cloud-tops is consistent with their non-detection in ground-

190 based images obtained in the 890 nm methane absorption band, since clouds reaching the
 191 tropopause at 60-100 mbar would be detected in that band [31]. The particles in the storm
 192 clouds are marginally brighter (i.e. with lower imaginary refractive index) and slightly
 193 larger (radius of 0.18 μm instead of 0.10 μm) relative to surrounding clouds, but such
 194 variations are within the 1-sigma retrieval error for these parameters. These properties are
 195 consistent with those found for storms observed in the “storm alley” in 2004-2009 as
 196 studied using Cassini/VIMS 1-5 μm spectra [32].
 197
 198



199
 200

201 **Figure 4. Vertical cloud structure and particle imaginary refractive index.** Radiative
 202 transfer model results based on HST images. (a) Particle density as a function of height
 203 (altitude increasing with decreasing pressure) in the storm and four different surrounding
 204 areas as indicated in the inset. The “a priori” particle density assumed for the model
 205 retrieval is also indicated; (b) Imaginary refractive index vs. wavelength for particles in
 206 the storm and in a surrounding area. See also Figure S5. The error band (particle
 207 density) and error bars (imaginary refractive index) are 1-sigma errors computed
 208 following [28-29].

209
 210
 211
 212
 213
 214
 215
 216
 217
 218
 219
 220
 221
 222
 223
 224
 225
 226
 227
 228
 229
 230
 231
 232
 233
 234
 235
 236
 237
 238
 239
 240
 241
 242
 243
 244
 245
 246
 247
 248
 249
 250
 251
 252
 253
 254
 255
 256
 257
 258

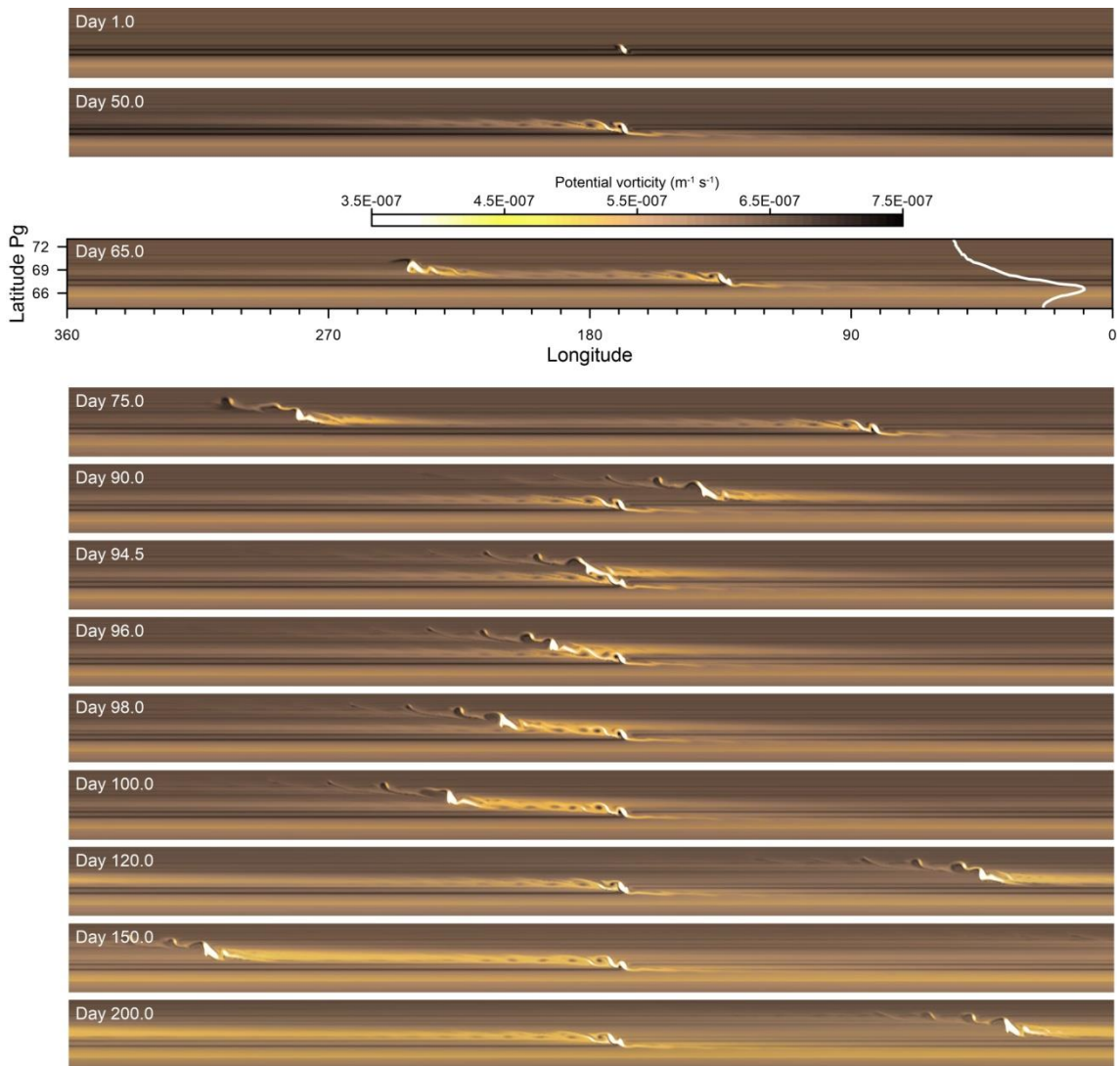
Dynamical simulations

In order to quantify the energy involved in the development of these storms, we have studied the dynamical effects on the atmospheric flow of simulated storms using a shallow water model (SW) [33] and the EPIC General Circulation Model [9, 34-35]. Both models represent simplified versions of Saturn's troposphere at the latitude where the storms developed. We simulated a latitudinal domain in which we imposed fluid motions that follow the measured wind profile (i. e. the zonal mean velocity as a function of latitude, Fig. 2). We introduce a convective storm in this flow as a localized disturbance with the measured size of the observed spots (WS1 and WS2) and with a certain intensity. In the SW model, the storm is initiated by a horizontal Gaussian mass flow with a given amplitude Q (m^3s^{-1}). In the EPIC model, the disturbance is introduced as a Gaussian heating source that injects a localized source of energy in the flow E (W kg^{-1}). In both cases, the mass flow amplitude (Q) and energy (E) and the duration of the disturbances, as well as their location in the wind profile (latitude and velocity), determine the evolution of the two-dimensional potential vorticity field (PV) [27] that can be compared to the observed cloud morphology [9, 33-35]. In our simulations, the amplitude of the mass injection or heating source are left as free parameters. Other adjustable parameters of the models are described in Methods section and Supplementary Tables 4.1 and 4.2.

In the SW model, we simulated the evolution of storms WS1 and WS2 and their mutual interaction. Our best fit between the observed WS1 and WS2 cloud morphology and the PV field given by the model requires a mass flow injection in the range $Q = 2-4 \times 10^9 \text{ m}^3\text{s}^{-1}$ (Figure 5). In the model, the encounter between WS1 and WS2 (days 94.5 – 100 in Fig. 5) generates a zonal disturbance that links both storms resembling the observations (Fig 1f-1h and Fig.1 map). The disturbed band between WS1 and WS2 contains periodic features with apparent wavelike nature, reminiscent of the observations (Fig. 5, day 100). The interaction between both storms in the model also favors the propagation of the activity poleward of the latitude of WS2 (days 96 – 120 in Fig. 5) as observed in the outbreak of WS3 and WS4 at higher latitudes (Fig. 1 d-h and j-k and Fig. 2). The resulting value of the mass flow is much lower than that used under the same numerical conditions to simulate the Great White Spots (GWS) [9, 33] $Q = 2-3 \times 10^{11} \text{ m}^3\text{s}^{-1}$ (for GWS1960); $1-3 \times 10^{12} \text{ m}^3\text{s}^{-1}$ (GWS1990); $2-5 \times 10^{11} \text{ m}^3\text{s}^{-1}$ (GWS2010). This means that WS1 and WS2 require about ~ 0.01 in mass flow compared to that necessary to produce the non-equatorial GWS cases (i.e. those closer in latitude to the present one) that erupted in the years 1960 and 2010. In Supplementary Fig. 6, we present simulations of WS1 for an ample range of values for Q and for three close but different latitudes in the wind profile. The figure shows how sensitive are model results to both parameters (Q and φ or zonal velocity), thus constraining the Q value required to form the storm.

In the EPIC model, we simulated the outbreaks of WS1 and WS2 as single convective sources. We also tested the case of an outbreak inside a cyclonic vortex, as it was observed in the case of WS1 (Fig. 3). In order to get a realistic PV field that resembles the observed cloud morphology, we require energy inputs $E = 1-1.5 \text{ W kg}^{-1}$ for the WS1 and WS2 storms, injected in a small region of size $\sim 150 \text{ km}$. In the simulations, the disturbance expands horizontally in few days, as shown in the PV field. In the case of the outbreak triggered within a cyclone (which we take 1,500 km long and 500 km wide), the required value for the storm is similar both in energy and in extension, but under these circumstances, the storm PV field remains linked to the cyclone (although expanding

259 around it) and the cyclone survives the eruption (Supplementary Fig. 7). The required
 260 energy is again much lower than that used under the same numerical conditions to
 261 simulate the GWS 2010 [9] of $E = 500\text{-}1000 \text{ W kg}^{-1}$ injected in a Gaussian region with a
 262 size $\sim 3,000 \text{ km}$. In Supplementary Fig. 8, we present simulations of WS1 triggered inside
 263 the cyclone for an ample range of values for E showing again how sensitive are model
 264 results to the energy injection, therefore constraining the E value required to form the
 265 storm. We conclude from both models that the best simulations of the cloud morphologies
 266 of WS1 and WS2 require disturbances with lower integrated amplitudes $\sim 0.01\text{-}0.001$ in
 267 mass flow (Q) and energy (E) than storms of the GWS type. The simulations also require
 268 that the injection occurs continuously at the latitude and velocity observed for WS1 and
 269 WS2 (within the uncertainty in error bars, see Table 1 and Fig. 5 caption).
 270
 271



272

273

274 **Figure 5. Numerical simulations of the disturbances generated by the storm outbreaks.**
 275 *Shallow water model for WS1 and WS2 with a temporal duration of 200 days; WS1*
 276 *(latitude 67.7°N , zonal velocity $+59.8 \text{ ms}^{-1}$, mass rate injection $Q = 4 \times 10^9 \text{ m}^3 \text{ s}^{-1}$), WS2*
 277 *(latitude 68.9°N , zonal velocity $= +14.2 \text{ ms}^{-1}$, mass rate injection $Q = 2 \times 10^9 \text{ m}^3 \text{ s}^{-1}$). On*
 278 *the frame corresponding to day 65, we include on the right the wind zonal profile portion*
 279 *covered by the simulation domain, with a velocity range in the 96 ms^{-1} to -12 ms^{-1} interval.*

280 *In the model, both disturbances are injected continuously, moving with respect to rotation*
281 *system III with the velocity that was measured on Saturn's atmosphere. For the sake of*
282 *figure readability, WS1 is placed on the center longitude in all frames except the 65 and*
283 *75 day frames, where the center of the domain is approximately in the middle between*
284 *the two storms. The interaction resulting from an encounter between both storms can be*
285 *seen in days 94.5 to 100.*

286

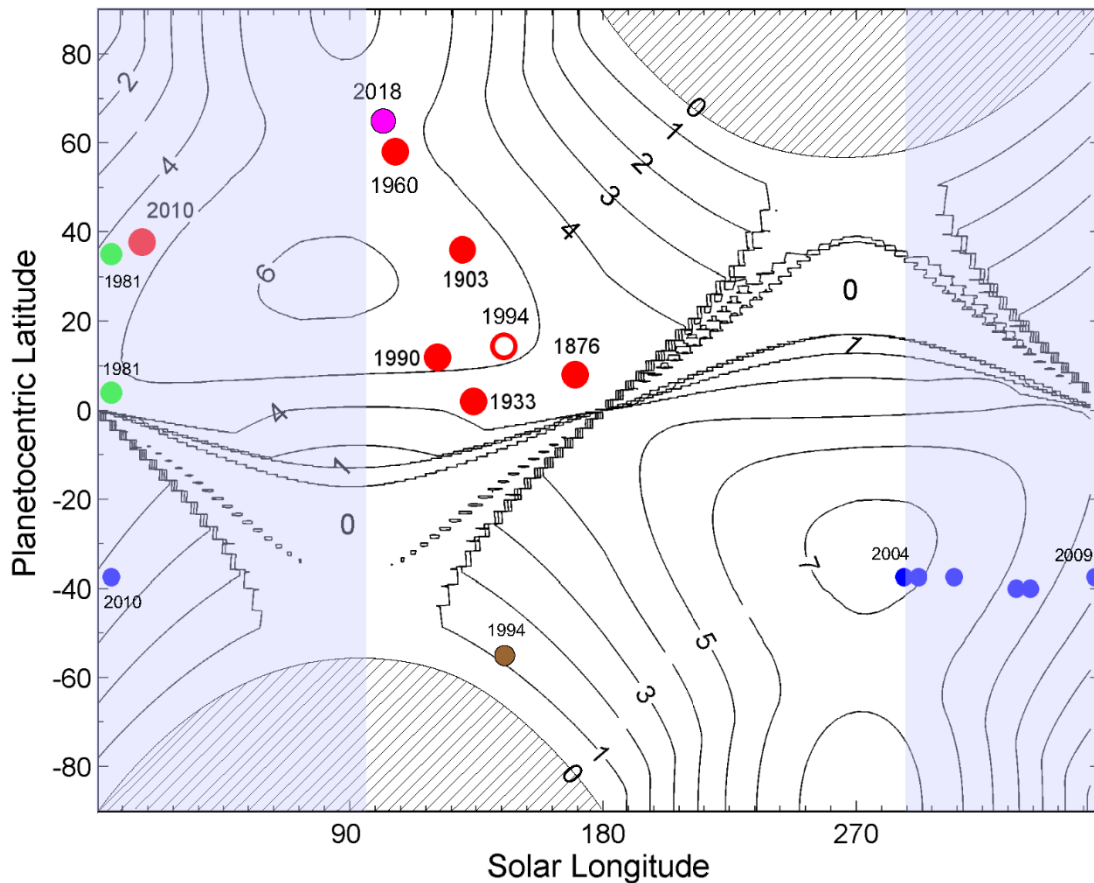
287 **Discussion**

288

289 The 2018 storms emerged at the same season on Saturn as the 1960 GWS (orbital
290 heliocentric longitude $L_s = 109^\circ$ for 1960 and 100° for 2018) (Fig. 6). The 1960 GWS
291 occurred southwards of WS1 at latitude $\sim +58^\circ$, i.e. on the equatorial side of the double
292 wind jet, moving with $u \sim 4 \text{ ms}^{-1}$ (Fig. 2) [6, 12]. The two main spots forming the 1960
293 GWS had a much larger zonal size of $\sim 35^\circ - 45^\circ$, that is, ~ 4 times the size of the 2018
294 WS1 and WS2 storms, and they grew faster than them, both in zonal and meridional
295 extension [36]. These properties, supported by the simulations described above, indicate
296 that the 2018 event was of lower intensity than the 1960 GWS. The 2018 storms could
297 have certain similarities with a middle size convective storm that occurred in 1994 at 56°S
298 [37]. That storm exhibited zonal expansion although the information we have for that case
299 is very scarce. On the other hand, the 2018 event is different from the kind of disturbance
300 that took place in 2015, which involved at least four vortices [25] and did not appear to
301 have a convective origin. We propose that the 2018 storms represent an intermediate case
302 of a convective disturbance between a classical GWS planetary-scale phenomenon and
303 the smaller-scale convective activity observed by Voyager 1 and 2 in 1980-81 [1-2, 5] and
304 by Cassini in 2004-2009 [10, 13-14, 19] (Fig. 6).

305

306



307

308

309

310

311

312

313

314

315

316

317

318

319

320

321

322

323

324

325

326

327

328

329

330

331

Figure 6. Seasonal insolation at the top of Saturn's atmosphere and convective events. Lines give the insolation in $W m^{-2}$ along a Saturn year represented in terms of the orbital heliocentric longitude (L_s), where $L_s=0^\circ$ is the northern vernal equinox, 90° is the northern summer solstice, 180° is the northern autumnal equinox and 270° is the northern winters solstice. The major convective storms, the Great White Spots are represented by red dots (year indicated [12]), including a large equatorial spot in 1994 (red circle [37]). The mid-scale storms were observed by Voyager 1 and 2 in 1980-81 (green [1-5]), with ground-based telescopes and HST in 1994 (brown, [37]) and with Cassini ISS in 2004-2010 (blue [10, 13-14, 16]). The 2018 storms are represented by the magenta dot (year indicated). The shaded polar region mark the nighttime periods. The blue area marks the period of full Cassini imaging coverage. In Supplementary Figure 9 we illustrate the visibility of Saturn disk due to changing geometry along the planet's orbit.

It is remarkable that the 2018 event emerged 58 years (~ 2 Saturn years = 58.89 years) after the GWS 1960, in agreement with the cycle observed in the equatorial GWSs [6, 12], as proposed by a coupled radiative-thermodynamic moist convection model [20]. The outburst of WS1 and WS2 follows the global 30-year cycle of all the observed GWS (except for the 2010 case that occurred in advance). We might speculate that the convective activity in 2018 was of lower intensity than that of 1960 due to the outbreak of the GWS 2010 at $38.2^\circ N$, which erupted about 7.3 years earlier and 30° to the south, and which could have altered the hypothetical cyclic properties of the GWSs. The lower intensity of WS1 and WS2 could be due to this previous outbreak, which could have limited the Convective Available Potential Energy (CAPE) [20, 27] and changed the

332 thermodynamic conditions in the region needed to favor a major storm outbreak. In any
 333 case, the intensity, planetary distribution and cyclic behavior of Saturn's convective
 334 storms represent a challenge in relation to the influence of the seasonal insolation and
 335 thermodynamic cycles in this complex multi-cloud-layer moist convective atmosphere.
 336

337 **Methods**

338 **Image data and measurement**

339
 340 Ground-based images used in this study were obtained employing the “lucky imaging”
 341 method [38]. Most telescopes employed were in the range 0.3-0.5 m in diameter (Table
 342 S1). D. Peach contributed a set of images obtained using “Chilescope”
 343 (<http://www.chilescope.com/>), a remotely controlled 1 m telescope. The images span the
 344 spectral ranges ~ 450 -650 nm (from color composites Red-Green-Blue, RGB) and the
 345 near infrared (~ 685 -980 nm), including a few obtained at the 890 nm-methane absorption
 346 band. The list of contributors to ALPO-Japan and PVOL2 databases whose images were
 347 used in this study is given Table 1 in the Supplementary Material. More than ~ 1500
 348 individual longitude–latitude feature measurements were acquired along the 353
 349 observing days. Images were navigated to fix Saturn disk using WinJupos free software
 350 [39] and in most cases reprocessed to increase the contrast of weak features. PlanetCam
 351 images, obtained with the 2.2 m Calar Alto telescope, cover two spectral ranges (visible,
 352 380-1,000 nm) and short wave infrared (SWIR, 1-1.7 μm) at specific selected
 353 wavelengths [23]. HST/WFPC images in this work span the wavelength range 225–763
 354 nm in selected spectral bands [24] (Supplementary Figure 5). The Cassini ISS images we
 355 employed to track back in time the position of the precursor cyclone to the first storm
 356 outbreak, were obtained in the MT3 filter (central wavelength 889 nm) between April and
 357 September 2017 [10] (Fig. 3). Strip maps of the region were constructed for identification
 358 and direct measurements of the images was performed using the PLIA software [41] and
 359 WinJupos (Supplementary Figure 1).

360

361

362 **Radiative transfer analysis**

363

364 HST images have been calibrated in absolute reflectivity following standard procedures
 365 [42]. For every image, the reflectivity values of the storm have been measured, as well as
 366 their emission and incidence angles. Such values were fitted to a Minnaert law [27, 29],
 367 and nadir-viewing reflectivity $(I/F)_0$ and limb darkening parameter k were retrieved. We
 368 computed the expected values of reflectivity for the storm using those Minnaert
 369 parameters for three geometries ($\mu=0.725$ and $\mu_0=0.786$; $\mu=0.555$ and $\mu_0=0.632$; $\mu=0.448$
 370 and $\mu_0=0.511$ (where μ is the cosine of the emission angle and μ_0 the cosine of the
 371 incidence angle). These values sample the observed positions of the disturbance within
 372 the plane-parallel approximation. Finally, we took as a reference the undisturbed
 373 background atmosphere at 69°N, close to the latitude of the storms. In order to capture
 374 the center to limb variation for the reference atmosphere, we selected 18 longitude points
 375 along this region covering in total 284° degrees in System III longitudes. Our goal was to
 376 reproduce the observed reflectivity and limb-darkening for all filters simultaneously, both
 377 for the storm and for the reference atmosphere. We used the radiative transfer code and
 378 retrieval suite NEMESIS [28], which uses the optimal estimator scheme to find the most
 379 likely model to explain the observations. This version of the code assumes a plane-parallel
 380 atmosphere for scattering, uses a doubling/adding scheme, and also considers the

381 Rayleigh scattering due to the mixture of H₂ and He as well as the absorption due to CH₄,
 382 with a volume mixing ratio of 4.7×10^{-3} relative to H₂ [43]. The thermal profile, which
 383 has little impact on the absorption coefficients at these wavelengths, was taken from [44]
 384 and extrapolated adiabatically. The overall assumptions and fitting strategy were the same
 385 as in a previous works [29, 45]. Supplementary Tables 2-3 give the values used for the a
 386 priori assumptions and best fitting results, respectively.

387

388 **Dynamical analysis and numerical simulations**

389 For the dynamical models, we used the wind profile measured with Cassini ISS [21] that
 390 is continuously forced. A parallel version of the SW model [33] was run with a resolution
 391 of 0.1 deg pix^{-1} and time step of 60 seconds, about one half of the maximum allowed by
 392 the Courant–Friedrichs–Lewy condition. Since the numerical integration is performed
 393 with fully explicit schemes, the parallelization with a domain-decomposition strategy is
 394 very efficient. The disturbance was kept active during the whole simulation time. The
 395 model uses periodic conditions in longitude and full-slip (reflective) in latitude. No
 396 topography is present. The EPIC model [34] was run with a horizontal resolution of
 397 $0.12 \times 0.06 \text{ deg pix}^{-1}$ and 5 vertical layers centered at a pressure level of 260 mbar. The
 398 vertical shear of the zonal wind was null across the layers and the Brunt-Väisälä
 399 frequency was set at $N = 0.007 \text{ s}^{-1}$ as in previous works in Saturn [9, 35]. In the SW model,
 400 the Rossby radius of deformation is $L_R = (gH)^{1/2}/f \sim 230 \text{ km}$, (gravity $g = 10 \text{ ms}^{-2}$, SW
 401 layer depth $H = 500 \text{ m}$, Coriolis parameter $f = 3.05 \times 10^{-4} \text{ s}^{-1}$), comparable to that obtained
 402 for the 2010 GWS ($200 \text{ km} \leq L_R \leq 600 \text{ km}$). Note that this Rossby deformation radius is
 403 the one used in the SW model (and not that of the real atmosphere). The Rossby
 404 deformation radius in the EPIC model is $L_R = NH/f \sim 1,000 \text{ km}$ ($H \sim 40 \text{ km}$ is the scale
 405 height). Further details of the range of values of the parameters used in the simulations
 406 are given in Supplementary Tables 4.1 and 4.2.

407

408 **Data availability.** This work relies in images that can be downloaded from the following
 409 sources (see Supplemengary Material for further details):

410 Association of Lunar and Planetary Observers ALPO – Japan:

411 <http://alpo-j.asahikawa-med.ac.jp/Latest/Saturn.html>

412 PVOL2 database: <http://pvol2.ehu.eus/pvol2/>

413 HST-OPAL program:

414 <https://archive.stsci.edu/prepds/opal/>

415 Cassini ISS images at NASA PDS (Planetary Data System):

416 <https://pds-imaging.jpl.nasa.gov/volumes/iss.html>

417 PlanetCam images are available from the corresponding author.

418

419 **Code availability.** The shallow water model code (ref. 19) is available from Enrique
 420 García-Melendo (enrique.garcia.melendo@upc.edu) upon request. The radiative transfer
 421 code NEMESIS (<http://users.ox.ac.uk/~atmp0035/nemesis.html>) is available upon request
 422 from Patrick Irwin (patrick.irwin@physics.ox.ac.uk). The EPIC numerical model (ref.
 423 32) is an open-code funded by NASA, see details:

424 http://surveygizmoreponseuploads.s3.amazonaws.com/fileuploads/15647/4054745/254-fd0a70105de25e281834d7f5dcc5451c_DowlingTimothyE.pdf

425

426

427

428

429

430 **References**

431

432 1. Smith, B.A, et al., Encounter with Saturn: Voyager 1 imaging results, *Science*, **212**,
433 163–191 (1981).

434

435 2. Smith, B.A, et al., A new look at the Saturn system: the Voyager 2 images, *Science*
436 **215**, 505–537 (1982).

437

438 3. Sromovsky, L. A., et al., Voyager 2 observations of Saturn's northern mid-latitude
439 cloud features: Morphology, motions, and evolution. *J. Geophys. Res.*, **88** (A11), 8650–
440 8666 (1983).

441

442 4. Ingersoll, A. P., Beebe, R. F., Conrath, B. J., & Hunt, G. E., Structure and dynamics of
443 Saturn's atmosphere, in *Saturn*, Gehrels, T., and M. S. Matthews, *University of Arizona*
444 *Press*, 195–238 (1984).

445

446 5. Sánchez-Lavega, A. Rojas J. F. & Sada, P.V. Saturn's zonal winds at cloud level,
447 *Icarus*, **147**, 405-420 (2000).

448

449 6. Sánchez-Lavega, A., Saturn's Great White Spots, *Chaos*, **4**, 341-353 (1994).

450

451 7. Sánchez-Lavega, A. et al. A strong decrease in Saturn's equatorial jet at cloud level,
452 *Nature*, **423**, 623-625 (2003).

453

454 8. Sánchez-Lavega, A., et al. Saturn's Cloud Morphology and Zonal Winds Before the
455 Cassini Encounter, *Icarus*, **170**, 519-523 (2004).

456

457 9. Sánchez-Lavega A., et al. Deep winds beneath Saturn's upper clouds from a seasonal
458 long-lived planetary-scale storm, *Nature*, 475, 71-74 (2011)

459

460 10. Porco, C.C., et al., Cassini Imaging Science: Initial results on Saturn's atmosphere,
461 *Science*, **307**, 1243-1247 (2005).

462

463 11. Sayanagi, K. M., et al., Dynamics of Saturn's great storm of 2010-2011 from Cassini
464 ISS and RPWS, *Icarus*, **223**, 460-478 (2013).

465

466 12. Sánchez-Lavega A. et al. *The Great Storm of 2010-2011*, Chapter 13 in *Saturn in the*
467 *21st Century*, eds. K. H. Baines, F. M. Flasar, N. Krupp, T. S. Stallard, Cambridge
468 University Press, pp. 377-416 (2019).

469

470 13. Dyudina, U. A., et al., Lightning storms on Saturn observed by Cassini ISS and RPWS
471 during 2004-2006, *Icarus*, **190**, 545-555 (2007).

472

473 14. Dyudina, U.A., et al., Detection of visible lightning on Saturn., *Geophys. Res. Lett.*,
474 **37**, L09205. (2010).

475

476 15. Fischer, G. et al., A giant thunderstorm on Saturn, *Nature*, **475**, 75-77 (2011).

477

- 478 16. Baines K. H., et al., Storm clouds on Saturn: Lightning-induced chemistry and
479 associated materials consistent with Cassini/VIMS spectra, *Planet. Space Sci.*, **57**, 1650-
480 1658 (2009).
481
- 482 17. Sánchez-Lavega, A., Battaner, E. The nature of Saturn's Great White Spots,
483 *Astronomy & Astrophysics*, **185**, 315-326 (1987).
484
- 485 18. Hueso, R., Sánchez-Lavega, A., A three-dimensional model of moist convection for
486 the giant planets II: Saturn's water and ammonia moist convective storms. *Icarus*, **172**,
487 255-271 (2004).
488
- 489 19. Del Genio A. D., Achterberg R. K., Baines K. H., Flasar F. M., Read P.L., Sánchez-
490 Lavega A., Showman A. P., Saturn Atmospheric Structure and Dynamics, Chapter 6 in
491 *Saturn after Cassini-Huygens*. M. Dougherty, L. Esposito and T. Krimigis (eds.),
492 Springer-Verlag, pp. 113-159 (2009).
493
- 494 20. Li, C. & Ingersoll, A. P., Moist convection in hydrogen atmospheres and the
495 frequency of Saturn's giant storms, *Nat. Geoscience*, **8**, 398-403 (2015).
496
- 497 21. García-Melendo, E. et al., Saturn's zonal wind profile in 2004 - 2009 from Cassini
498 ISS images and its long-term variability, *Icarus*, **215**, 62-74 (2011).
499
- 500 22. Hueso R., et al., The Planetary Virtual Observatory and Laboratory (PVOL) and its
501 integration into the Virtual European Solar and Planetary Access (VESPA), *Planet. Space*
502 *Sci.*, **150**, 22-35 (2018).
503
- 504 23. Mendikoa I., et al. PlanetCam UPV/EHU: A two channel lucky imaging camera for
505 Solar System studies in the spectral range 0.38-1.7 μm , *Pub. Astron. Soc. Pacific*, **128**,
506 035002, 22 pp (2016).
507
- 508 24. Simon, A. A., Wong, M. H., Orton, G. S., First Results from the Hubble OPAL
509 Program: Jupiter in 2015, *Astrophys. J.*, **812**, 51S (2015).
510
- 511 25. del Rio-Gaztelurrutia T. et al., A planetary-scale disturbance in a long living three
512 vortex coupled system in Saturn's atmosphere, *Icarus*, **302**, 499-513 (2018).
513
- 514 26. Fletcher, L. N., et al., Moist convection and the 2010–2011 revival of Jupiter's South
515 Equatorial Belt, *Icarus*, **286**, 94-117 (2017).
516
- 517 27. Sánchez-Lavega, A., An Introduction to Planetary Atmospheres, Taylor-Francis,
518 CRC Press, Florida, pp. 629 (2011)
519
- 520 28. Irwin, P.G.J. et al., The NEMESIS planetary atmosphere radiative transfer and
521 retrieval tool, *J. Quant. Spectrosc. Radiat. Transf.*, **109**, 1136–1150 (2008)
522
- 523 29. Sanz-Requena, J.F., et al., Haze and cloud structure of Saturn's North Pole and
524 Hexagon Wave from Cassini/ISS imaging, *Icarus*, **305**, 284-300 (2018).
525

- 526 30. Sánchez-Lavega A., Pérez-Hoyos S., Hueso R., Condensate clouds in planetary
527 atmospheres: a useful application of the Clausius-Clapeyron equation, *Amer. J. Physics*,
528 **72**, 767-774 (2004).
529
- 530 31. West R. A., Baines K. H., Karkoschka E. and Sánchez-Lavega A., Clouds and
531 Aerosols in Saturn's Atmosphere. Chapter 7 in *Saturn after Cassini-Huygens*. M.
532 Dougherty, L. Esposito and T. Krimigis (edt.), Springer-Verlag, pp. 161-179 (2009).
533
- 534 32. Sromovsky L. A., Baines K. H. & Fry P.M., Models of bright storm clouds and related
535 dark ovals in Saturn's Storm Alley as constrained by 2008 Cassini/VIMS spectra, *Icarus*,
536 **302**, 360-385 (2018).
537
- 538 33. García-Melendo E. & Sánchez-Lavega, A., Shallow Water simulations of Saturn's
539 Giant Storms at different latitudes, *Icarus*, **286**, 241-260 (2017).
540
- 541 34. Dowling, T.E., The Explicit Planetary Isentropic-Coordinate (EPIC) atmospheric
542 model, *Icarus*, **132**, 221-238 (1998).
543
- 544 35. García-Melendo, E., et al., Atmospheric dynamics of Saturn's 2010 giant storm,
545 *Nature Geos.*, **6**, 525-529 (2013).
546
- 547 36. Dollfus, A., Mouvements dans l'Atmosphère de Saturne en 1960. Observations
548 coordonnées par l'Union Astronomique Internationale, *Icarus*, **2**, 109-114 (1963).
549
- 550 37. Sánchez Lavega, A. et al., Large-scale storms in Saturn's atmosphere during 1994,
551 *Science*, **271**, 631 – 634 (1996)
552

553 **Methods References**

- 554
- 555 38. Mousis O., et al., Instrumental Methods for Professional and Amateur Collaborations
556 in Planetary Astronomy, *Experimental Astronomy*, **38**, 91-191 (2014).
557
- 558 39. WinJUPOS: <http://www.grischa-hahn.homepage.t-online.de/> (accessed 2018)
559
- 560 40. Porco, C.C., et al., Cassini Imaging Science: Instrument characteristics and
561 anticipated scientific investigations at Saturn, *Space Sci. Rev.*, **115**, 363-497 (2004).
562
- 563 41. Hueso, R., et al., The Planetary Laboratory for Image Analysis (PLIA), *Adv. Space*
564 *Res.*, **46**, 1120-1138 (2010).
565
- 566 42. Dressel, L., Wide Field Camera 3 Instrument Handbook, Version 10.0, Space Tel.
567 Science Inst., Baltimore (2018).
568
- 569 43. Fletcher, L.N. et al., Methane and its isotopologues on Saturn from Cassini/CIRS
570 observations, *Icarus*, **199**, 351 – 367 (2009).
571
- 572 44. Lindal, G.F. et al., The atmosphere of Saturn – an analysis of the Voyager radio
573 occultation measurements, *Astronomical Journal*, **90**, 1136 – 1146 (1985)
574

575 45. Pérez-Hoyos, S. et al., Saturn's tropospheric particles phase function and spatial
576 distribution from Cassini ISS 2010-11 observations, *Icarus*, 277, 1 – 18 (2016)

577

578 **Acknowledgements**

579

580 This work has been supported by the Spanish project AYA2015-65041-P
581 (MINECO/FEDER, UE) and Grupos Gobierno Vasco IT-765-13. A list of the sources for
582 the images used in this paper can be found in the Supporting Information. This work used
583 data acquired from the NASA/ESA HST Space Telescope, associated with OPAL
584 program (PI: Simon, GO13937), and archived by the Space Telescope Science Institute,
585 which is operated by the Association of Universities for Research in Astronomy, Inc.,
586 under NASA contract NAS 5-26555. All OPAL maps are available at
587 <http://dx.doi.org/10.17909/T9G593>, and MHW and AAS acknowledge financial support
588 from his program. M.H.W. through a grant from the Space Telescope Science Institute,
589 which is operated by AURA under NASA contract NAS 5-26555.

590

591

592 **Author contributions**

593

594 ASL directed the work, made the features tracking measurements, retrieved the winds,
595 and interpreted the results; EGM, MS and JL performed the shallow water and EPIC
596 numerical simulations; TdR performed the Cassini image analysis of the storm precursor;
597 RH, JMG, TB, MDe contributed to the analysis of ground-based observations; JFSR and
598 SPH performed the radiative transfer analysis; AAS and MHW performed the HST
599 observations and helped in their analysis; KMS, JJB and JLG mapped and analyzed
600 Cassini ISS images; UD and SE designed the ISS observation sequences. All authors
601 discussed the results and contributed to preparing the manuscript.

602

603 **Competing interests**

604 The authors declare no competing financial interests.

605

606 **Additional information**

607 Supplementary information is available for this paper at